An Iron-Calcium-Miro Axis Influences Parkinson's Risk and Neurodegeneration

Vinita Bharat[1], Roeland Vanhauwaert[1], Li Li[1], Colin M. Muir[2,3], Aarooran Sivakumaran Durairaj[1], Sujyoti Chandra[1], Yann Le Guen[4,5], Pawan Nandakishore[6], Chung-Han Hsieh[1], Stefano E. Rensi[7], Russ B. Altman[7], Michael D. Greicius[4], Liang Feng[2], and Xinnan Wang[1]*

Affiliations:

1. Department of Neurosurgery, Stanford University School of Medicine, Stanford, CA94305, USA;
2. Department of Molecular and Cellular Physiology, Stanford University School of Medicine, Stanford, CA94305, USA;
3. Graduate Program of Molecular and Cellular Physiology, Stanford University School of Medicine, Stanford, CA94305, USA;
4. Department of Neurology and Neurological Sciences, Stanford University School of Medicine, Stanford, CA94305, USA;
5. Institut du Cerveau - Paris Brain Institute - ICM, 75013, Paris, France;
6. Vroom Inc., Houston, TX77042, USA;
7. Department of Bioengineering, Stanford University, Stanford, CA94305, USA.

* Correspondence: xinnanw@stanford.edu

Summary

Genetic backgrounds and risk factors among individuals with Parkinson's disease (PD) are highly heterogenous, limiting our ability to effectively detect and treat PD. Here we connect several potential PD risk genes and elements to one biological pathway. Elevation of Fe^{2+}-levels causes Ca^{2+}-overflow into the mitochondria, through an interaction of Fe^{2+} with mitochondrial calcium uniporter (MCU), the Ca^{2+}-import channel in the inner mitochondrial membrane, and resultant MCU oligomerization. This mechanism acts in PD neuron models and postmortem brains. Miro, a Ca^{2+}-binding protein, functions downstream of Ca^{2+}-dysregulation, and holds promise to classify PD status and monitor drug efficacy in human blood cells. Polygenetic enrichment of rare, non-synonymous variants in this iron-calcium-Miro axis influences PD risk. This axis can be targeted by multiple ways to prevent neurodegeneration in PD models. Our results show a linear pathway linking several PD risk factors, which can be leveraged for genetic counseling, risk evaluation, and therapeutic strategies.

Main Text

Introduction

Parkinson's disease (PD) is a leading cause of disability, afflicting the aging population. The dopamine (DA)-producing neurons in the substantia nigra are the first to die in PD patients. A bottleneck that hinders our ability to effectively detect and treat PD may be the presence of highly heterogenous genetic backgrounds and risk factors among different patients. More than 90% of the PD cases are considered sporadic with no known causal mutations. Genome-wide association studies (GWAS) have identified over 90 risk loci (Diaz-Ortiz et al., 2022). Functional studies on known causal genes of familial patients and from cellular and animal PD models have pointed to multiple "cellular risk elements", such as mitochondrial damage, lysosomal dysfunction, immune system activation, neuronal calcium mishandling,

and iron accumulation (Angelova et al., 2020; Apicco et al., 2021; Belaidi and Bush, 2016; Buttner et al., 2013; Kim et al., 2020; Lee et al., 2018; Surmeier et al., 2017; Tabata et al., 2018; Verma et al., 2017; Vuuren et al., 2020). These distinct genetic and cellular risk factors may confer individual heterogeneity in disease onset, but also suggest that there are networks and pathways linking these "hubs" in disease pathogenesis. Identifying their connections could be crucial for finding a cure for PD.

Mitochondria are the center of cellular metabolism and communication. Ions such as calcium and iron, are not only essential for diverse mitochondrial functions but can be stored inside the mitochondria to maintain cellular ionic homeostasis. Ion channels in the plasma and mitochondrial membranes coordinate for ion uptake, transport, and storage. For example, calcium ions enter the cell via voltage- or ligand-gated calcium channels across the cell surface. Inside the cell, they are taken up by mitochondria through the outer mitochondrial membrane (OMM) channel, VDAC, and the inner mitochondrial membrane (IMM) channel, mitochondrial calcium uniporter (MCU) (Baughman et al., 2011), and extruded into the cytosol through the IMM transporter, NCLX (Palty et al., 2010). MCU is a multimeric holocomplex consisting of additional regulatory subunits, such as essential MCU regulator (EMRE), mitochondrial calcium uptake 1 (MICU1), MICU2, and MCUb (Fan et al., 2018; Fan et al., 2020; Lambert et al., 2019). Channels complementary to these major mitochondrial calcium channels also exist (Patron et al., 2022). It remains a mystery regarding the relation of calcium and iron ions in PD mechanisms and their contribution to disease susceptibility.

Identifying the cellular causes to neuron death will not only provide more effective disease management but also shed light on molecular signatures shared by a subset of people affected by the disease. A convenient, cost-effective method to spot the vulnerable population, even before the symptom onset, will

be extremely valuable for early intervention and preventive medicine. It will improve the efficacy of clinical trials for testing experimental drugs, by facilitating patient stratification and serving as a pharmacodynamic marker.

Understanding disease-causing cellular paths will also help us zoom in on rare genetic variants that contribute to disease etiology but otherwise are difficult to discover through GWAS. Integrating studies of risk variants with disease models and human tissues could establish a causal link of a biological pathway to a disease with complex traits such as PD, with the promise of identifying more effective druggable targets and biomarkers. In this work, we harness the power of combining human genetics, cellular and in vivo models, and patient's tissues, and identify an iron-calcium-Miro axis in PD. Iron accumulation causes mitochondrial calcium overload via promoting MCU oligomerization and its channel activity, which may consequently disturb cellular calcium homeostasis. Miro, a calcium-binding protein, acts downstream of calcium dysregulation in PD models. Functional and genetic impairments in this axis may increase PD risk and indicate PD status.

Results

A high-content Miro1 screening assay identifies a network of Ca^{2+}-related drug hits for PD

Miro is an OMM protein essential for mediating mitochondrial motility and safeguarding their quality. Human Miro1 and Miro2 are paralogs with high sequence similarity. We have previously shown that in fibroblasts or neurons derived from sporadic and familial PD patients, Miro1 degradation upon mitochondrial depolarization is delayed, consequently slowing mitophagy and increasing neuronal sensitivity to stressors (Hsieh et al., 2019; Hsieh et al., 2016; Shaltouki et al., 2018). This Miro1 phenotype would serve as an excellent readout for screening small molecules that promote Miro1 degradation

following depolarization. Many compounds in the commonly used screening libraries have well-defined roles and targets, and some show efficacy to treat certain human diseases. This rich information may allow us to reveal cellular pathways underlying the Miro1 phenotype in PD. To this end, we established a sensitive immunocytochemistry (ICC)-based assay that was suitable for high-throughput screening (Figures 1A, S1, S2, S3A, more details in Method). We performed the primary screens at the Stanford High-Throughput Bioscience Center (HTBC) using 3 drug libraries in a sporadic PD fibroblast line. Overall, we identified 35 actives (1.92% primary hit rate) that reduced Miro1 following mitochondrial depolarization (Figure S1, Table S1A-B). To validate the results of the high-content assays, we retested 34 out of the 35 positive Miro1 reducers identified at the Stanford HTBC in our own laboratory using fresh compounds and our confocal microscope. We confirmed that 15 compounds reliably reduced Miro1 protein levels following mitochondrial depolarization in PD fibroblasts (Figure S2, Table S1C). Next, we performed a pathway analysis using a knowledge graph-based tool to reveal the potential cellular pathways connecting Miro1 to each hit compound. Strikingly, we discovered intracellular Ca^{2+} as a primary shared factor in the hit drug-Miro1 network (Figure 1B, Table S2). Two drugs, Benidipine and Tranilast, could directly inhibit plasma membrane Ca^{2+}-channels. Benidipine is a blocker of voltage-gated Ca^{2+}-channels (L-, N-, T-type), and Tranilast has been proposed to inhibit ligand-gated Ca^{2+}-channels (TRPV2) (Darakhshan and Pour, 2015). Dysregulation of Ca^{2+} homeostasis has been widely reported in PD models (Angelova et al., 2020; Apicco et al., 2021; Buttner et al., 2013; Kim et al., 2020; Lee et al., 2018; Surmeier et al., 2017; Tabata et al., 2018; Verma et al., 2017). Our results suggest a direct link of the Ca^{2+}-binding protein, Miro, to Ca^{2+}-mediated abnormality in PD.

Validation of a role for Benidipine in Miro degradation

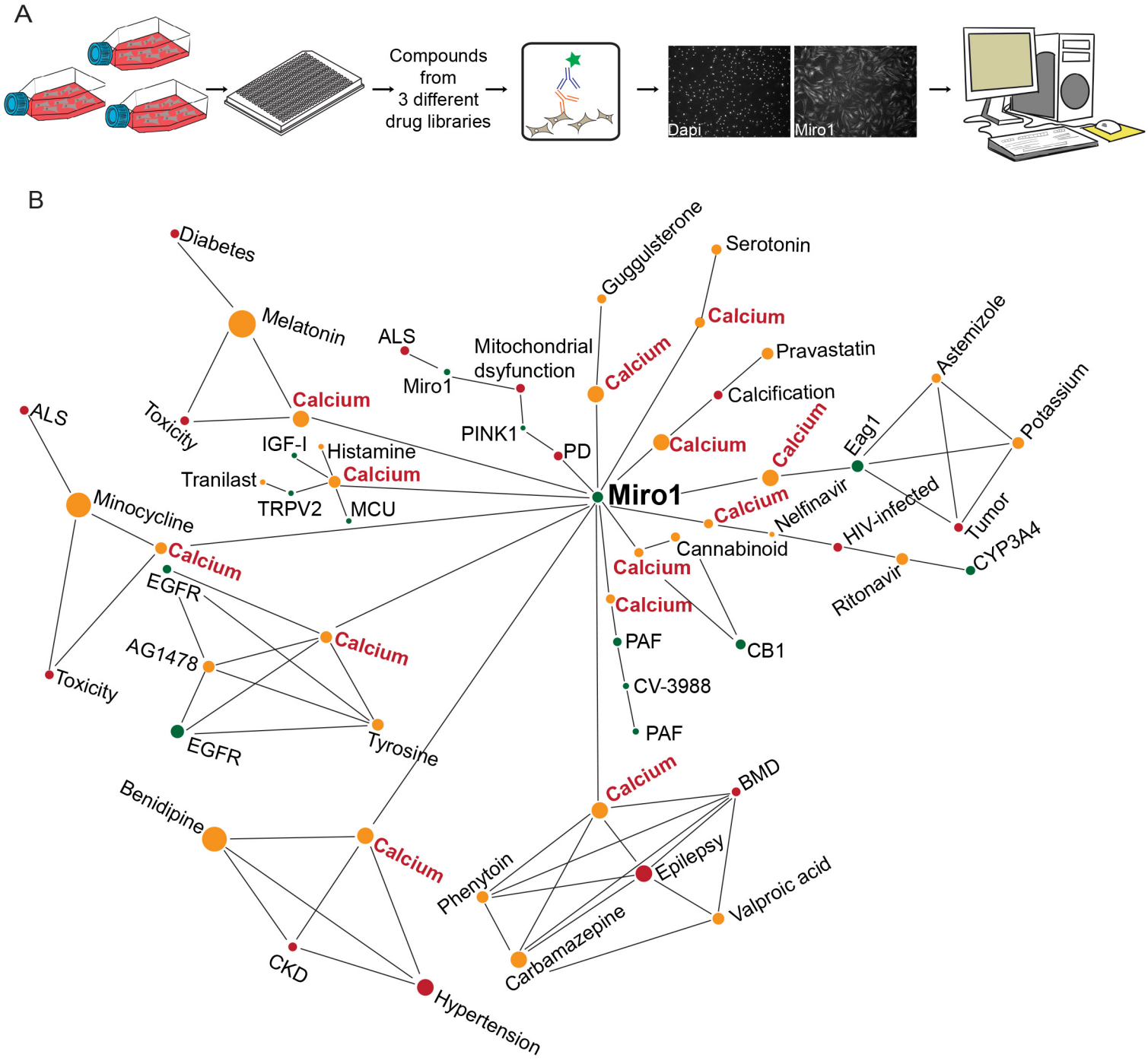

Figure 1. HTP Screens Identify Calcium-Related Drug Hits for PD. (A) Schematic representation of a custom-designed drug screen for Miro1 in PD fibroblasts. (B) Pathway analysis identified calcium as a shared factor in the primary hit-Miro1 network. Each individual pathway is generated using a primary hit and Miro1 as search query and the resulting subnetwork is visualized and curated using docs2graph–a knowledge-graph browser. The visualization shows a subgraph generated by docs2graph from the collection of curated supporting documents for each pathway.

To understand in detail the relation of Miro with the Ca^{2+}-pathway in Parkinson's pathogenesis, we further examined Benidipine's role in Miro protein stability. Using the same ICC method as in Figure S2, we found that Benidipine reduced Miro1 in a dose-dependent manner in PD fibroblasts treated with carbonyl cyanide 4-(trifluoromethoxy)phenylhydrazone (FCCP) (Figure S3B). To exclude the possibility of any artifacts caused by our ICC method, we verified our results using an entirely different approach to detect Miro1 response to depolarization. We measured Miro1 and additional mitochondrial proteins by Western blotting. We also depolarized mitochondria with a different uncoupler, carbonyl cyanide *m*-chlorophenyl hydrazone (CCCP) (Hsieh et al., 2019), instead of FCCP. We detected Miro1 and mitochondrial markers at 6 and 14 hours after CCCP treatment. We have previously demonstrated that in healthy control fibroblasts following CCCP treatment, Miro1 is degraded earlier (6 hours) than multiple other mitochondrial markers (14 hours) (Figure S3C) (Hsieh et al., 2019; Hsieh et al., 2016), consistent with the observation of proteasomal degradation of Miro1 prior to mitophagy (Chan et al., 2011; Hsieh et al., 2019; Hsieh et al., 2016; Wang et al., 2011). Using this alternative method, we confirmed that both Miro1 degradation and damaged mitochondrial clearance were impaired in the PD cell line we used for screens. Importantly, Benidipine promoted Miro1 degradation after 6 hours following CCCP treatment without affecting the matrix protein ATP5β and facilitated mitochondrial clearance as was evidenced by the degradation of both Miro1 and ATP5β at 14 hours post-treatment (Figure S3C). Interestingly, Miro2 was also resistant to depolarization-induced degradation in PD cells (Hsieh et al., 2019) and Benidipine rescued its phenotype (Figure S3C). This result suggests that Miro1 and Miro2, which share the Ca^{2+}-binding EF-hands, are functionally redundant in the Ca^{2+}-dependent regulation. We confirmed that Benidipine did not affect *Miro1* messenger RNA (mRNA) expression detected by reverse transcription quantitative real-time PCR (RT-qPCR) under basal and depolarized conditions in PD cells (Figure S3D). Neither did Benidipine alter the basal ATP levels (Figure S3E), nor the mitochondrial membrane potential

137 measured by TMRM staining (Figure S3F). Collectively, we have demonstrated that Benidipine, a Ca^{2+}-
138 channel blocker, specifically promotes Miro degradation upon depolarization in PD fibroblasts using
139 multiple methods.
140
141 **Benidipine rescues Parkinson's phenotypes in human neuron and fly models of PD**
142 We have previously shown that reducing Miro rescues Parkinson's phenotypes in cellular and in vivo
143 models (Hsieh et al., 2019; Hsieh et al., 2016; Li et al., 2021; Shaltouki et al., 2018), suggesting that small
144 molecules that lower Miro protein levels could represent an effective therapeutic approach for PD. From
145 our high-throughput screens we have discovered that Benidipine, which targets the Ca^{2+} pathway,
146 promotes Miro degradation upon depolarization in skin cells of a PD patient (Figures 1, S1-3). We next
147 tested whether Benidipine was useful for alleviating Parkinson's phenotypes in two independent models:
148 the human neuron and fly models. We examined Benidipine using induced pluripotent stem cells (iPSCs)
149 from one familial patient with the A53T mutation in *SNCA* (encodes α-synuclein) and its isogenic wild-
150 type control (Hsieh et al., 2019; Hsieh et al., 2016; Li et al., 2021; Shaltouki et al., 2018). We differentiated
151 iPSCs to neurons expressing tyrosine hydroxylase (TH), the rate-limiting enzyme for DA synthesis as
152 previously described (Figure S4A) (Hsieh et al., 2019; Hsieh et al., 2016; Li et al., 2021; Shaltouki et al.,
153 2018). These patient-derived neurons display increased expression of endogenous α-synuclein (Shaltouki
154 et al., 2018). We identified DA neurons by TH-immunostaining and cell death by terminal
155 deoxynucleotidyl transferase dUTP nick end labeling (TUNEL)-staining (Li et al., 2021; Shaltouki et al.,
156 2018) (Figures 2A-B, S4A). We have previously shown that iPSC-derived DA neurons from PD patients
157 are more vulnerable to stressors than those from healthy controls (Hsieh et al., 2019; Hsieh et al., 2016;
158 Li et al., 2021; Shaltouki et al., 2018). The treatment of the complex III inhibitor, Antimycin A, at 10 μM
159 for 6 hours caused acute neuronal cell death leading to the loss of TH and the increase of TUNEL signals

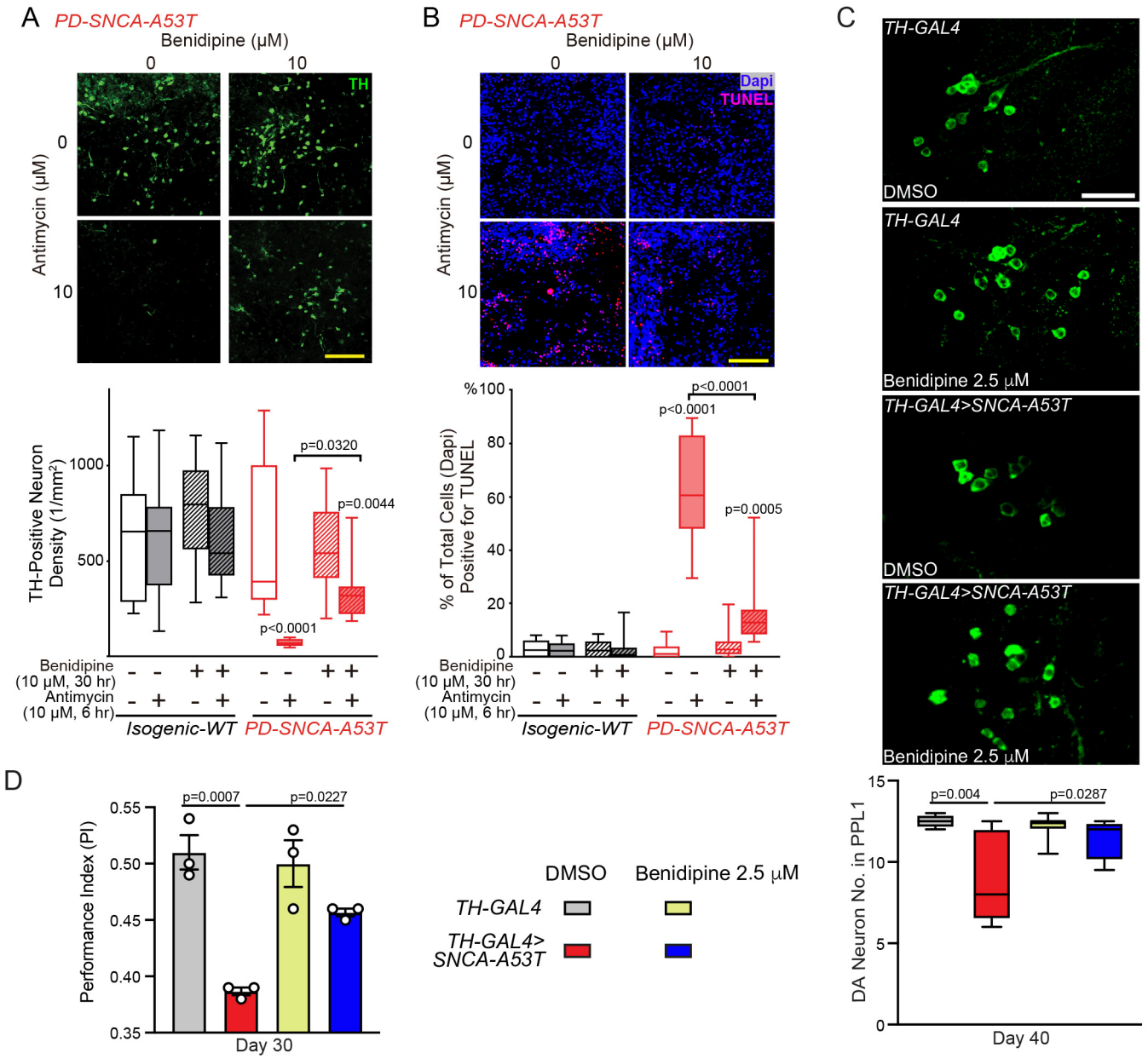

Figure 2. Benidipine Rescues PD Relevant Phenotypes. (A-B) iPSC-derived neurons from a PD patient with SNCA-A53T and the isogenic control, treated as indicated, were immunostained with anti-TH (A) or TUNEL and Dapi (B), and imaged under a confocal microscope. Scale bars: 100 um. Below: Quantifications of the density of TH-positive neurons (A) or the percentage of TUNEL-positive neurons (B). n=20 images from 3 independent coverslips. P values are compared with the far-left bar, except indicated otherwise. (C) 40-day-old fly brains were immunostained with anti-TH and the DA neuron number was counted in the PPL1 cluster. Scale bar: 20 um. n=4, 7, 7, 4 (from left to right). (D) The Performance Index was measured in 30-day-old flies, fed as indicated. n=59, 57, 54, 57 flies (from left to right), 3 independent experiments. (C-D) Drug treatment was started from adulthood (day 1). One-Way Anova Post Hoc Tukey Test for all panels.

in neurons derived from the PD patient (Hsieh et al., 2019; Li et al., 2021; Shaltouki et al., 2018) (Figure 2A-B). Notably, Benidipine treatment at 10 μM for 30 hours significantly rescued this stressor-induced neuron death (Figure 2A-B).

In order to cross-validate the neuroprotective effect of Benidipine in vivo, we fed Benidipine to a fly model of PD, which expressed the pathogenic human α-synuclein protein with the A53T mutation (α-syn-A53T) in DA neurons driven by *TH-GAL4* (Hsieh et al., 2019; Li et al., 2021; Shaltouki et al., 2018). These flies exhibit PD-relevant phenotypes such as age-dependent locomotor decline and DA neuron loss (Hsieh et al., 2019; Li et al., 2021; Shaltouki et al., 2018). Importantly, feeding PD flies with 2.5 μM Benidipine from adulthood prevented DA neuron loss in aged flies (Figure 2C) and improved their locomotor ability (Figure 2D). Taken together, Benidipine, which eliminates the Miro1 defect in PD fibroblasts, rescues PD-related phenotypes in human neuron and fly models.

The EF-hands of Miro play a role in causing Parkinson's-relevant phenotypes

Having demonstrated a link between Miro and Ca^{2+} in multiple models of PD, we next determined whether Ca^{2+} directly interacted with Miro to contribute to phenotypes in these models. To achieve this goal, we made GFP-tagged human Miro1 protein in both the wild-type (Miro1-WT) form and in a mutant form where two point mutations were introduced in the two EF-hands of Miro1 (Miro1-KK) to block Ca^{2+}-binding (Wang and Schwarz, 2009). We expressed GFP-tagged Miro1 (WT or KK) and Mito-dsRed that labeled mitochondria in iPSC-derived neurons from the PD patient and isogenic control, described earlier. We chose the distal segment of the axon for analysis (Hsieh et al., 2016). We have previously shown that following 100 μM Antimycin A treatment that triggers mitophagy, Miro1 and mitochondria are sequentially degraded in wild-type neurons (Hsieh et al., 2019; Hsieh et al., 2016; Shaltouki et al., 2018). We observed the same mitochondrial events in isogenic control axons transfected with GFP-Miro1-WT.

Within 25 min GFP-Miro1-WT was partially degraded, and within 58 min mitochondrial clearance was induced (Figure 3A-C). In contrast, in PD neuron axons transfected with GFP-Miro1-WT, the degradation rates of both Miro1 and damaged mitochondria upon Antimycin A treatment were slowed (Figure 3A-C), consistent with our previous studies (Hsieh et al., 2019; Shaltouki et al., 2018). Notably, GFP-Miro1-KK significantly rescued these phenotypes in PD axons: it expedited the degradation rates to the control level (Figure 3A-C). These data suggest that Miro1 directly binds to Ca^{2+} to mediate mitochondrial phenotypes in PD neurons, at least in part.

To confirm the Miro-Ca^{2+} relation in vivo, we generated transgenic flies carrying T7-tagged fly Miro (DMiro)-WT or DMiro-KK. DMiro is an ortholog of human Miro1 and Miro2. Both DMiro-WT and DMiro-KK were expressed at comparable levels when the transgenes were driven by the ubiquitous driver *Actin-GAL4* (Figure S4B). We next crossed these transgenic flies to a fly PD model described earlier that expressed human α-syn-A53T in DA neurons driven by *TH-GAL4*. Consistent with the results from human neurons, DMiro-KK significantly rescued the PD-relevant phenotypes including the age-dependent DA neuron loss and locomotor decline, as compared to DMiro-WT (Figure 3D-E). Altogether, we have provided evidence showing that the Ca^{2+}-binding domain of Miro plays a key role in causing phenotypes in human neuron and fly models of PD.

The Ca^{2+}-uptake ability of mitochondria is enhanced in PD neurons

Our results, showing that either blocking Ca^{2+}-entry into the cell or inhibiting Ca^{2+}-binding to Miro rescues the Miro and neurodegenerative phenotypes in PD models (Figures 1-3), placed Ca^{2+} dysregulation upstream of Miro. We next dissected how Ca^{2+}-handling was mis-regulated in neurons derived from the PD patient (Figures 2-3). We stimulated these neurons with the G-protein-coupled receptor (GPCR) agonist, thrombin, and measured cytosolic and mitochondrial Ca^{2+} levels with live Calcium Green and

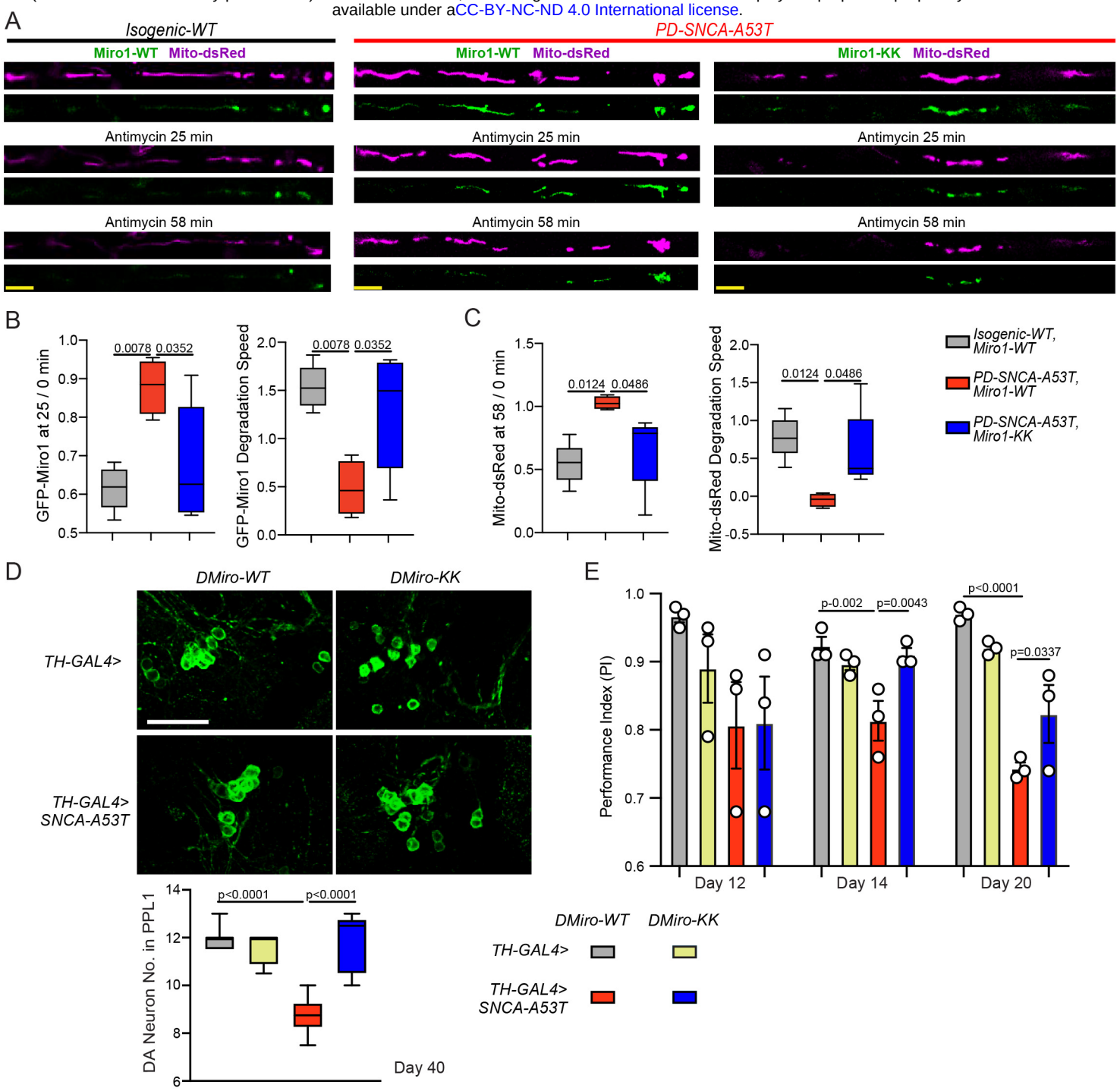

Figure 3. The EF-hands of Miro Play a Role in Causing PD Relevant Phenotypes. (A) Representative still images from live Mito-dsRed and GFP-Miro1 imaging movies of axons of indicated genotypes, following 100 uM Antimycin A treatment. Scale bar: 10 um. (B) Left: Quantification of the GFP-Miro1 intensity at 25 minutes divided by that at 0 minute following 100 uM Antimycin A treatment from the same axonal region. Right: Quantification of the reduction speed of the GFP-Miro1 intensity within 25 minutes following 100 uM Antimycin A treatment. (C) Left: Quantification of the Mito-dsRed intensity at 58 minutes divided by that at 0 minute following 100 uM Antimycin A treatment from the same axonal region. Right: Quantification of the Mito-dsRed intensity reduction speed within 58 minutes following 100 uM Antimycin A treatment. (B-C) n=5, 4, 5 (from left to right) axons (one axon per coverslip). (D) The DA neuron number was counted in the PPL1 cluster of flies with indicated genotypes. Scale bar: 20 um. n=7, 4, 6, 5 (from left to right). (E) The Performance Index was measured in flies with indicated genotypes and age. n (from left to right)=49, 47, 40, 47 flies (day 12); 49, 47, 39, 47 (day 14); 48, 45, 37, 44 (day 20); 3 independent experiments. One-Way Anova Post Hoc Tukey Test for all panels.

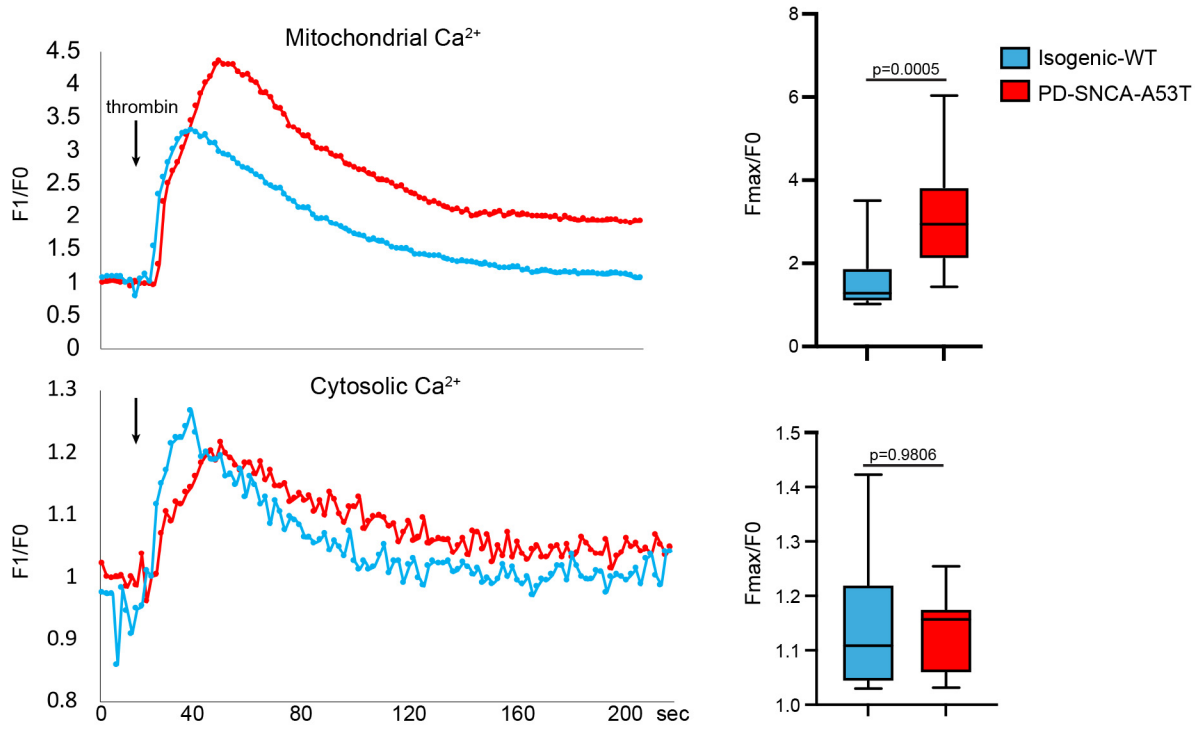

Figure 4. PD Mitochondria Import More Ca2+. iPSC-derived neurons from a PD patient with SNCA-A53T and the isogenic control were stimulated with thrombin and mitochondrial (Rhod-2) and cytosolic Ca2+ levels (Calcium Green) were measured. Left: Representative traces of Ca2+ ions in neurons. Right: Quantifications of the peak fluorescent intensity normalized to baseline. n=15 cell bodies from 3 independent coverslips. Two-tailed Welch's T Test.

206 Rhod-2 staining, respectively. We found that thrombin triggered intracellular Ca^{2+} mobilization and
207 elevation, which was comparable between PD and isogenic control neurons (Figure 4). However,
208 mitochondria in PD neurons sustained significantly larger Ca^{2+}-elevation after thrombin stimulation, as
209 compared to control (Figure 4). These results indicate that the mitochondrial Ca^{2+}-import ability is boosted
210 in PD neurons.
211
212 **Iron promotes the assembly of MCU oligomers**
213 The enhanced mitochondrial Ca^{2+}-uptake observed in PD neurons (Figure 4) led us to investigate the Ca^{2+}-
214 uptake channel in the IMM–MCU. The oligomerization of MCU is essential for MCU's function to import
215 Ca^{2+} into the mitochondria (Dong et al., 2017; Fan et al., 2018; Fan et al., 2020). We hypothesized that
216 MCU oligomerization could be affected by small molecules in the mitochondrial microenvironment,
217 particularly those with a role in PD, including Ca^{2+} (Figure 4), reactive oxygen species (ROS), and iron
218 (Belaidi and Bush, 2016). To explore this possibility, we performed size exclusion chromatography (SEC),
219 where protein complexes with higher molecular weight (MW) are eluted faster than those with lower MW,
220 using lysates of HEK cells treated with Fe^{2+}, Ca^{2+}, or H_2O_2. Detecting MCU from cell lysates using SEC
221 has been successfully shown (Dong et al., 2017; Lambert et al., 2019; Tomar et al., 2016). We found that
222 Fe^{2+}, Ca^{2+}, and H_2O_2 treatment all shifted the MCU elution peaks to the earlier fractions of higher-order
223 oligomers compared to control (Figure 5A, S4C-G; anti-MCU was validated in Figure S4C). In contrast,
224 the elution pattern of Miro1 was largely unaltered by any of these treatments (Figure S4D-G). These
225 results show that intracellular small molecules including iron, Ca^{2+} (Fan et al., 2020), and H_2O_2 (Dong et
226 al., 2017) can influence the equilibrium of MCU oligomeric complexes and may consequently alter the
227 MCU channel activity.

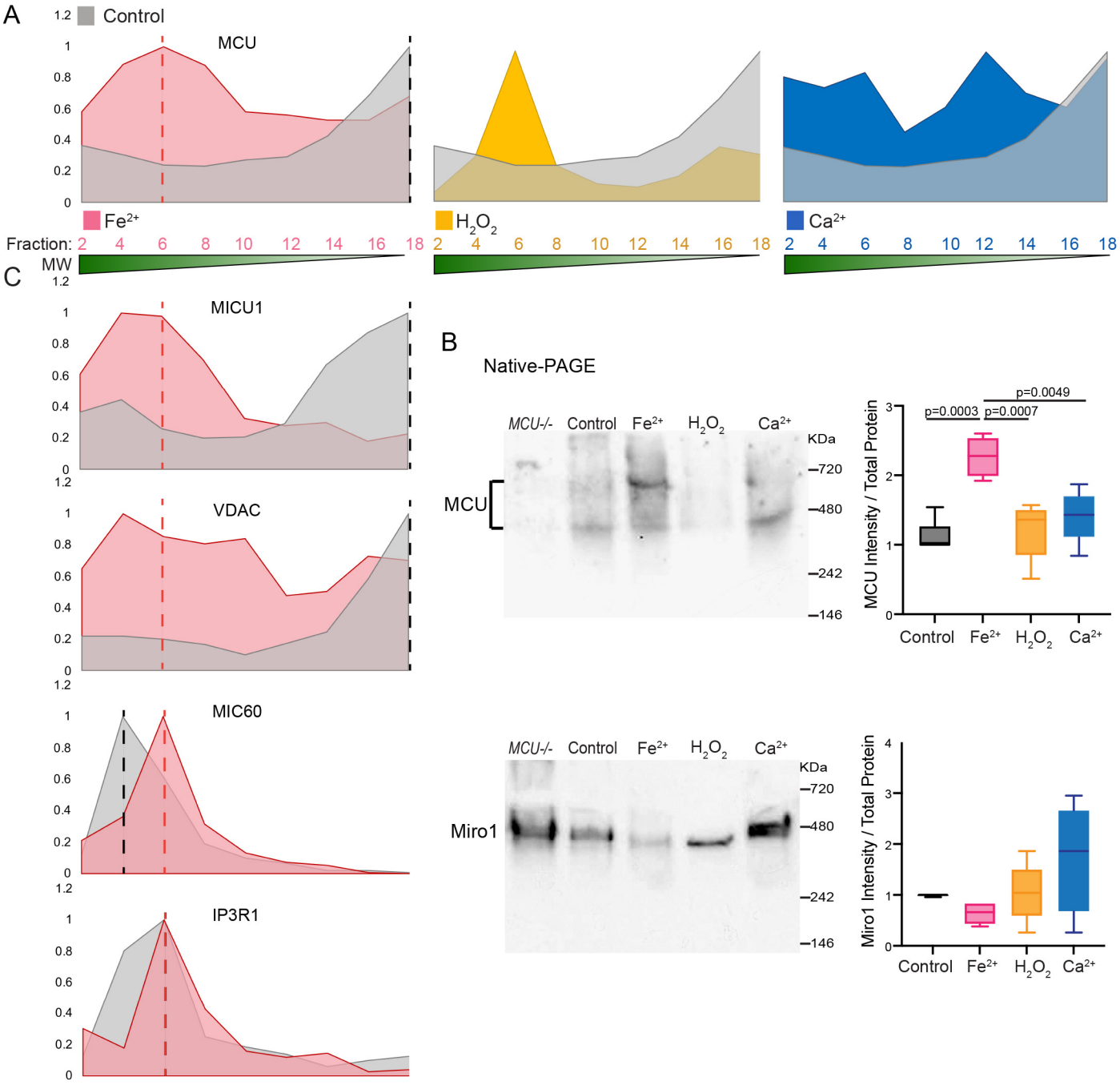

Figure 5. Iron Promotes MCU Oligomerization. (A) Elution profiles of MCU from SEC samples. (B) HEK cells were treated similarly as above, run in Native-PAGE, and blotted. Right: Qualifications of the band intensities normalized to the total protein amount measured by BCA. n=5 independent experiments. One-Way Anova Post Hoc Tukey Test. (C) Elution profiles of additional proteins from SEC samples.

SEC is a sensitive method to detect protein composition dynamics, while Native-PAGE can determine the overall form and amount of a multimeric native protein. The human MCU oligomer bands from HEK cells migrated between 400-700 KDa in Native-PAGE (Figure 5B; the negative control in the left lane, *MCU-/-,* showed no signal) (Baughman et al., 2011; Ghosh et al., 2020; Tomar et al., 2016). Importantly, we found that Fe^{2+} treatment, but not Ca^{2+} or H_2O_2, resulted in an increase in the total intensity of the MCU oligomer bands (Figure 5B). Miro1 protein also oligomerized and migrated as a single band around 480 KDa in Native-PAGE, which was not significantly affected by any of these treatments (Figure 5B). These data indicate that iron not only shifts the MCU complexes to higher-order oligomers but also enlarges the total number of these complexes, and thus may have a more profound impact on the MCU activity than Ca^{2+} and H_2O_2.

We next examined additional membrane proteins that may assist the MCU function using HEK cells. By detecting total protein levels using Western blotting, we found when Fe^{2+} was added in media and lysis buffer, MCUb and NCLX were lowered, but not any other proteins examined (Figure S5). MCUb is an inhibitor of MCU (Lambert et al., 2019), and NCLX is an IMM exchanger believed for mitochondrial Ca^2-extrusion (Lee et al., 2016; Palty et al., 2010). The reduction of both proteins could exacerbate the phenotype of mitochondrial Ca^{2+}-overload. By evaluating oligomeric dynamic changes using SEC, we found that the OMM channel, VDAC, and MCU's gating regulator, MICU1, showed a matching elution pattern with MCU, and the treatment of Fe^{2+} shifted all 3 proteins to the similar earlier fractions of higher order oligomers, which coincided with the elution peak of MIC60, a core structural protein at the crista junctions and contact sites (Zerbes et al., 2012), and IP3R1, the major ER Ca^{2+}-channel that delivers Ca^{2+} to the OMM (Katona et al., 2022) (Figure 5A, C). These data are consistent with VDAC, MICU1, and MCU being associated in the same super-complexes and suggest a possible spatial reorganization of the MCU super-complexes upon iron elevation, thus allowing easier access to ER Ca^{2+} supply. Taken together,

our results show that iron promotes MCU oligomerization and may cause Ca^{2+}-accumulation inside the mitochondria.

Fe^{2+} binds to the MCU complex and acts on its Ca^{2+}-import ability

We probed the mechanism underlying the observed impact of iron on MCU oligomerization (Figure 5A-B). One hypothesis was that the MCU complex bound to iron leading to conformational changes. To explore this possibility, we immunoprecipitated (IP) endogenous MCU from HEK cells and detected the iron concentrations in the IP samples. We found significantly more Fe^{2+} ions pulled down with MCU when HEK cells were treated with Fe^{2+}, compared with other controls (Figure 6A). This result shows that the MCU complex interacts with Fe^{2+}. To determine whether MCU directly bound to Fe^{2+}, we switched our experiments to an in vitro setting. To circumvent the problem of precipitation caused by a fast speed of Fe^{2+} oxidation in vitro, we used an Fe^{2+} mimic, Co^{2+} ion (Billesbolle et al., 2020). We first confirmed that Co^{2+} behaved similarly as Fe^{2+} in our functional assays in HEK cells: Co^{2+} treatment increased MCU oligomerization detected by Native-PAGE (Figure 6B), just like Fe^{2+} (Figures 5B, 6B), and both Fe^{2+} and Co^{2+} treatment enhanced the mitochondrial Ca^{2+}-uptake ability following thrombin application (Figure 6C). Using fluorescence-detection SEC on purified human MCU protein (Fan et al., 2020), we found that Co^{2+} caused the formation of higher-order oligomers of MCU, and decreased MCU protein stability with increased temperature (Figure 6D-E). These results demonstrate that the Fe^{2+} mimic, Co^{2+}, directly binds to MCU, increasing its oligomerization.

We next searched for amino acid residues in the matrix domain of MCU (PDB: 5KUE) predicted to bind to Fe^{2+} using an in-silico program (http://bioinfo.cmu.edu.tw/MIB/) (Lin et al., 2016; Lu et al., 2012), and found 3 amino acids: 74D, 148D, and 159H. The latter 2 residues were also predicted to bind to Co^{2+}. We mutated these 3 sites to Alanine (named "MCU-3A"). Indeed, we detected significantly less Fe^{2+}

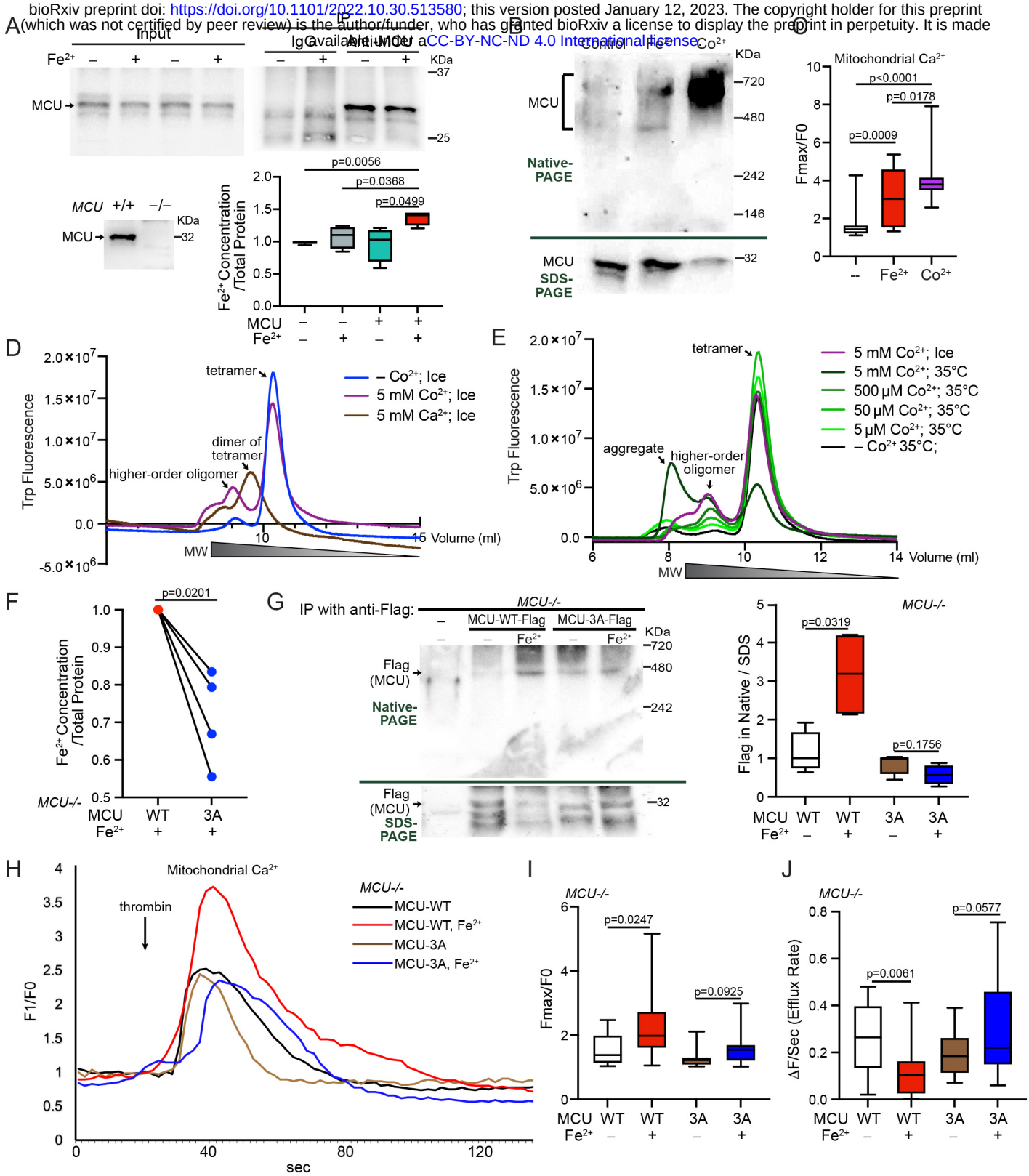

Figure 6. MCU Binds to Fe2+. (A) HEK cells were treated with or without 5 mM Fe2+ for 21 hours, then IPed with rabbit IgG or anti-MCU, and Fe2+ concentrations in the IP samples were detected. n=4 independent experiments. Top western blots demonstrated the success of IP. Anti-MCU was validated using MCU-/- HEK cell lysate (bottom panel). Arrow indicates the MCU band. (B) HEK cells were treated with 5 mM Fe2+ or Co2+ for 22 hours and lysed in buffer containing the same metal. Lysates were run in Native- or SDS-PAGE and blotted with anti-MCU. Similar results were seen for at least 3 times. (C) HEK cells treated with 5 mM Fe2+ or 500 µM Co2+ for 22 hours were stimulated with thrombin and mitochondrial Ca2+ levels (Rhod-2) were measured. The peak fluorescent intensity normalized to baseline is quantified. n=20 cells from 4 independent coverslips. (D-E) Fluorescence-detection SEC profiles of purified human MCU. The annotation of the peaks is based on (Fan et al., 2018; Fan et al., 2020). (F) MCU-/- HEK cells transfected as indicated were treated with 5 mM Fe2+ for 20 hours, then IPed with anti-Flag, and Fe2+ concentrations in the IP samples were detected. Two-tailed paired T Test. (G) Left: Representative blots of IP with anti-Flag using cell lysates as indicated, run in Native- or SDS-PAGE. Right: Quantification of the band intensity of MCU-Flag in Native-PAGE normalized to that in SDS-PAGE from the same experiment. n=4 independent experiments. (H) HEK cells treated as indicated were stimulated with thrombin and mitochondrial Ca2+ levels (Rhod-2) were measured. Representative traces of Ca2+ ions. (I-J) Based on traces like in (H), the peak fluorescent intensity normalized to baseline (I) or efflux rate (J) is quantified. n=17 cells from 4 independent coverslips. Two-tailed Welch's T Test for all panels except (F).

bound to Flag-tagged MCU-3A, as compared to MCU-WT, produced from HEK cells without endogenous MCU (*MCU-/-*) (Figure 6F). To determine whether these mutations were sufficient to eliminate the Fe^{2+}-triggered oligomerization of MCU, we expressed MCU-WT or MCU-3A in *MCU-/-* HEK cells, treated these cells with Fe^{2+}, and ran the IPed proteins in Native-PAGE. As expected, MCU-3A abolished MCU's response to Fe^{2+} treatment: the MCU oligomer band intensity was no longer increased (Figure 6G). We then live imaged mitochondrial Ca^{2+}-dynamics, as described in Figure 4, in these cells. We consistently observed a larger mitochondrial Ca^{2+}-elevation following thrombin stimulation in MCU-WT-transfected HEK cells treated with Fe^{2+} as compared to no Fe^{2+}-treatment, and MCU-3A blunted the peak increase (Figure 6H-I). Because Fe^{2+} also lowered NCLX levels (Figure S5) which could affect mitochondrial Ca^{2+}-extrusion, we measured the mitochondrial Ca^{2+}-efflux rate. Indeed, Fe^{2+} treatment slowed the efflux rate, which was prevented by MCU-3A (Figure 6J), suggesting that the Fe^{2+}-triggered efflux delay might depend on Ca^{2+}-overload. Altogether, our results show that Fe^{2+} binds to the MCU complex, promoting MCU oligomerization and its channel activity.

Iron functions upstream of calcium to mediate phenotypes of PD neurons

Our discovery of the action of Fe^{2+} on the MCU activity (Figures 5-6) suggested that in PD neurons, the phenotype of mitochondrial Ca^{2+}-overload (Figure 4) might depend on iron. To confirm their causal relation, we treated PD neurons with deferiprone (DFP), an iron chelator (Munson et al., 2021). Indeed, DFP significantly reduced mitochondrial Ca^{2+}-accumulation following thrombin stimulation (Figure 7A) and prevented cell death triggered by Antimycin A treatment (Figure 7B) in iPSC-derived neurons from the familial PD patient described earlier. We treated neurons from a second, sporadic patient with DFP and saw a similar neuroprotective effect (Figure 7B). In vivo, feeding the fly model of PD as shown earlier (Figures 2-3) with DFP consistently rescued the PD-relevant phenotypes, including age-dependent DA

297 neuron loss and locomotor decline (Figure 7C-D). Collectively, our results show that iron functions
298 upstream of calcium to mediate neurodegeneration in PD models.
299
300 **MCU, MCUb, and NCLX are affected in PD postmortem brain**
301 Our finding showing that iron impacts mitochondrial Ca^{2+}-channels and transporters (Figure 5, 6B, S5)
302 prompted us to examine these proteins in postmortem brains of people with PD, diffuse Lewy body disease
303 (DLBD), or Alzheimer's disease (AD) (Table S3). We homogenized the frontal cortex and ran the brain
304 lysate in Native- or SDS-PAGE. We focused on MCU oligomers, NCLX, and MCUb, which were shown
305 earlier specifically altered by Fe^{2+} treatment in HEK cells (Figure 5B, 6B, S5). We found the PD group
306 clustered and separated from the healthy control group, with higher intensity of the MCU oligomer bands
307 and lower intensity of both the NCLX and MCUb bands (Figure 7E), similar to the observations in HEK
308 cells treated with Fe^{2+} (Figure 5B, 6B, S5). This unique clustering was not observed in the AD or DLBD
309 group (Figure 7E, S6). Together, our data suggest that the combined functional impairment of MCU,
310 MCUb, and NCLX may be one of the molecular signatures shared by people with PD.
311
312 **Miro1 in blood cells reflects PD status and responds to drug treatment**
313 Now we have demonstrated a functional axis of iron-calcium-Miro in neurons of our PD models and
314 patients. We next sought evidence of its impairment in peripheral tissues of PD patients, which could
315 serve as an excellent candidate for biomarker and pharmacodynamic marker development. Measuring the
316 combined impairment of MCU oligomerization, MCUb, and NCLX requires a large amount of protein
317 and Native-PAGE, which is not applicable for high-throughput screening and clinical practice. We then
318 explored Miro1, whose slower degradation following mitochondrial depolarization was downstream of
319 Ca^{2+}-dysregulation in our PD models, as shown earlier (Figures 1-3). Notably, we have previously found

that in skin fibroblasts and iPSCs the delay of Miro1 degradation upon depolarization distinguishes PD patients and genetic carriers from healthy controls (Hsieh et al., 2019; Hsieh et al., 2016; Nguyen et al., 2021). Although fibroblasts can be readily obtained by a skin biopsy, a blood test remains the most convenient method. We investigated whether Miro1 could be detected in peripheral blood mononuclear cells (PBMCs) acquired from a blood draw. We cultured PBMCs from a healthy donor from the Stanford Blood Center (SBC, Table S4) and depolarized the mitochondrial membrane potential using two different methods: Antimycin A plus Oligomycin (Ordureau et al., 2020), or CCCP. We found that both depolarizing approaches caused the degradation of Miro1 and additional mitochondrial markers in a time-dependent manner, detected by Western blotting (Figure S7A-B), consistent with other cell types (Hsieh et al., 2019; Hsieh et al., 2016; Nguyen et al., 2021).

To enable high-content screening, we applied an enzyme-linked immunosorbent assay (ELISA) of Miro1 (Figure S7C-D) to PBMCs from the same donor with 6-hour CCCP treatment. We saw a similar Miro1 response to CCCP using ELISA (SBC, Table S4). We then used this ELISA to screen a total of 80 healthy controls and 107 PD patients (Table S4). Miro1 Ratio (Miro1 protein value with CCCP divided by that with DMSO from the same person) was significantly higher in PD patients compared to healthy controls (Figure 7F, Table S4), indicating that Miro1 is more stable upon depolarization in PD patients.

To determine whether our method could be used to classify an individual into a PD or healthy group, we employed machine learning approaches using our dataset. We trained a logistic regression model to assess the impact of Miro1 Ratio on PD diagnosis, solely on its own or combined with additional demographic and clinical parameters (Method). Unified Parkinson's Disease Rating Scale (UPDRS) is a tool to measure motor and non-motor symptoms of PD which may reflect disease severity and progression. Using UPDRS, our model yielded an accuracy (an individual was correctly classified as with PD or healthy) of 81.2% ($p<0.000001$; area under the Receiver Operator Curve (ROC)–AUC=0.822), and using

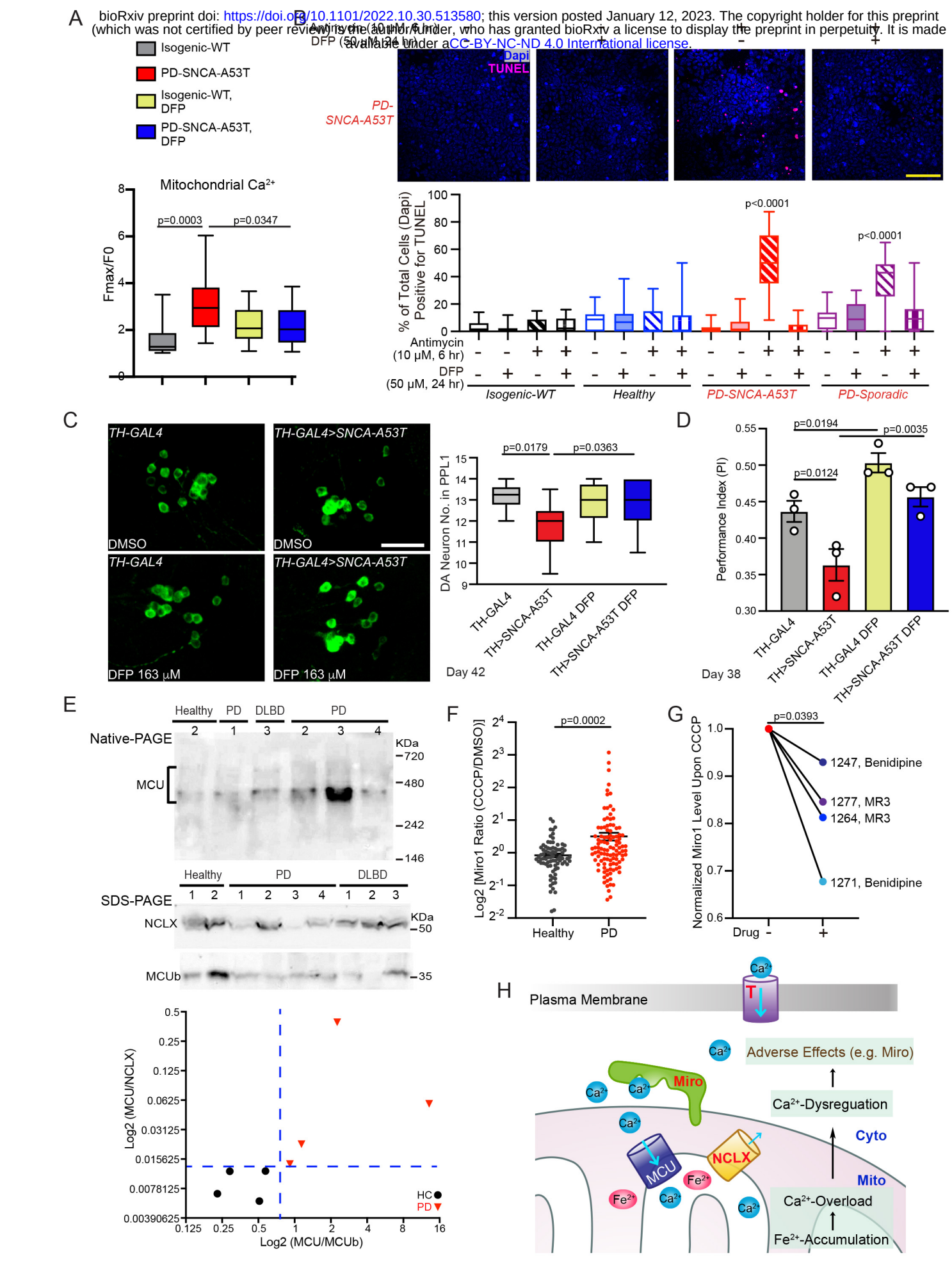

Figure 7. Chelating Iron Restores Ca2+ and neuronal homeostasis in PD neurons. (A) Similar to Figure 4, iPSC-derived neurons from a PD patient with SNCA-A53T and the isogenic control, with or without treatment of 100 uM DFP for 24 hours, were stimulated with thrombin, and mitochondrial Ca2+ (Rhod-2) was measured. Quantifications of the peak fluorescent intensity normalized to baseline. n=15 cell bodies from 3 independent coverslips. Control data without DFP treatment are the same as in Figure 4. One-Way Anova Post Hoc Tukey Test. (B) iPSC-derived neurons treated as indicated, were immunostained with TUNEL and Dapi, and imaged under a confocal microscope. Scale bar: 50 um. Below: Quantification of the percentage of TUNEL-positive neurons. n=20 images from 3 independent coverslips. P values are compared within each genotype (significant compared to every other condition) with One-Way Anova Post Hoc Tukey Test. (C) The DA neuron number was counted in the PPL1 cluster of flies with indicated genotypes and conditions. Drug treatment was started from adulthood (day 1). Scale bar: 20 um. n=6, 9, 8, 7 (from left to right). (D) The Performance Index was measured in flies. Drug treatment was started from embryogenesis. n=35, 33, 40, 34 flies (from left to right), 3 independent experiments. (C-D) One-Way Anova Post Hoc Tukey Test. (E) Postmortem brains were run in Native- or SDS-PAGE and blotted. The band intensity normalized to the total protein level measured by BCA is divided by that of the universal control on the same blot: CVD (cardiovascular disease), which was included on every blot. The MCU oligomer bands in Native-PAGE and the NCLX and MCUb bands in SDS-PAGE (average of 3 replicates) are used in the plot. HC: healthy control. (F) Miro1 protein levels were measured using ELISA in PBMCs treated with DMSO or 40 uM CCCP for 6 hours. Miro1 Ratio is calculated by dividing the Miro1 value treated with CCCP by that with DMSO from the same subject. Dot plot with Mean±S.E.M. n=80 healthy controls and 107 PD. Two-tailed Welch's T Test. (G) PBMCs from 4 PD patients were treated with 40 uM CCCP for 6 hours, or pretreated with 10 uM Benidipine or MR3 for 18 hours and then with 40 uM CCCP for another 6 hours, and Miro1 protein was detected using ELISA. Patient IDs are the same as in Table S4. Two-tailed paired T Test. (H) Schematic representation of the iron-calcium-Miro axis discovered in this study. Red texts show genes containing variants associated with PD status.

Miro1 Ratio, the accuracy was 67.6% (p=0.03; AUC=0.677). Notably, if both Miro1 Ratio and UPDRS were considered, our model generated an improved accuracy of 87.8% (p=0.02; AUC=0.878), without the interference of age or sex (Method, Figure S7E-F). Therefore, our results suggest that the molecular (Miro1 Ratio) and symptomatic (UPDRS) evaluations may reveal independent information, and that combining both tests may more accurately categorize individuals with PD and measure their responses to experimental therapies.

To probe the potential utilization of this Miro1 assay in future clinical trials for stratifying patients or monitoring drug efficacy, we treated PBMCs from 4 PD patients (Table S4) with either of the two compounds known to reduce Miro1, Benidipine (Figures 1-2, S2) and Miro1 Reducer 3 (MR3) (Hsieh et al., 2019; Li et al., 2021). Miro1 protein levels upon CCCP treatment were lowered by each compound in all 4 patients (Figure 7G), showing that the Miro1 marker in PBMCs can respond to drug treatment. Collectively, our results suggest that Miro1 protein in blood cells may be used to aid in diagnosis and drug development.

Rare variants in the iron-calcium-Miro pathway are associated with PD status

After dissecting the functional impairment of this iron-calcium-Miro axis in PD, we explored its genetic contribution to PD. Earlier, we showed that chelating iron, blocking Miro's binding to Ca^{2+}, or preventing Ca^{2+}-entry into the cell all alleviated parkinsonian neurodegeneration (Figures 2, 3, 7). We evaluated the genes encoding the protein targets of these approaches, which are spatially distinct and localized to three subcellular locations: (1) IMM Ca^{2+}-channels and transporters (targeted by Fe^{2+}), (2) the Ca^{2+}-binding protein Miro on the OMM, and (3) plasma membrane Ca^{2+}-channels (targeted by Benidipine and Tranilast) (Figure 7H, Table S5). By analyzing common variants within or near any of the investigated genes in GWAS reported in (Nalls et al., 2019), we did not observe significant association with PD clinical status.

We next employed the whole-genome sequencing (WGS) data from the Accelerating Medicines Partnership–Parkinson's Disease (AMP–PD) (1,168 control; 2,241 PD), and assessed rare non-synonymous and damaging variants using burden based and SKATO methods. We discovered polygenetic vulnerability to PD at all three spatial hotspots: significant association with PD status of rare variants in selective T-type Ca^{2+}-channel subtypes (*Cav3.2*, *3.3*) (cell surface), *Miro2* (OMM), and *NCLX* (IMM) (Table S5). A SKATO Test on all variants of T-type or L-type Ca^{2+}-channel subtypes consistently showed significant association with PD status of T-type channels, which survived multiple comparison correction, but not of L-type channels (Table S5). Together, our analysis unravels genetic predisposition of this Ca^{2+}-pathway to PD.

To functionally validate the selection of T-type Ca^{2+}-channels from our human genetic study, we employed the same screening ICC assay described earlier (Figures S1-2) by which we discovered the non-selective pan-Ca^{2+}-channel blocker, Benidipine, but now using 2 different specific L-type and 3 different T-type Ca^{2+}-channel blockers. Intriguingly, we again discovered a striking selection of T-type versus L-type channels, in the connection with Miro1 in PD fibroblasts (Figure S7G): only T-type blockers promoted Miro1 degradation following depolarization, just like Benidipine, supporting the human genetic finding. Similar to Miro1, Miro2 was also resistant to depolarization-triggered degradation in PD fibroblasts (Hsieh et al., 2019) and responded to Benidipine treatment (Figure S3C). NCLX functionally interacts with MCU (Lee et al., 2016), and was coregulated with MCUb and MCU by Fe^{2+} (Figure 5B, 6B, S5) and PD (Figure 7E). Although it remains elusive why rare variants in these genes are selectively associated with PD status, our combined, unbiased analyses of human genetics, tissues, cell, and in vivo models corroborate the complexity and multifactorial nature of PD etiology, and indicate that the polygenetic architecture built around this iron-calcium-Miro axis might influence an individual's risk to develop PD.

Discussion

In this work, we have established a pathway of iron-calcium-Miro dysregulation in our PD models (Figure 7H). Elevation of iron concentrations may cause mitochondrial Ca^{2+}-overload by promoting the MCU activity and reducing NCLX levels (Figures 4-7, S5). It is possible that the initial mitochondrial Ca^{2+}-accumulation subsequently disrupts Ca^{2+}-homeostasis at the cellular level, eliciting responses of additional Ca^{2+}-binding proteins, such as Miro (Figure 7H). We have shown multiple ways to target this axis. Chelating iron, reducing Ca^{2+}-entry into the cell, or blocking Miro's binding to Ca^{2+} is each neuroprotective (Figures 2, 3, 7). Of note, the impairment of this axis can be reflected in blood cells using a Miro1 assay with high content capacity (Figure 7F-G) and can be detected in the genome of PD patients (Table S5). Hence, this ionic axis may be important for PD pathogenesis and can be leveraged for better detecting and treating the disease.

Although the precise course of PD pathogenesis remains unclear, emerging evidence has demonstrated its complex and polygenetic nature. Interactions among multiple organs and cell types, systemic immune activation, and environmental triggers act uniquely in different individuals. Although GWAS and segregation studies have unveiled many PD risk or causal loci, rare genetic variants may be particularly important for conferring individual heterogeneity in disease onset and etiology. However, rare variants associated with PD risk are difficult to discover given the limitations in sample collection and the unmet need for exome-sequencing as opposed to sparse genotyping on microarrays. In our work, we have located several potential risk genes by first connecting them in the same biological pathway. In an individual prone to PD, there might be already mitochondrial malfunction causing mitochondrial proteins to release labile iron, or impairments in systemic iron uptake and circulation causing iron accumulation at the cellular

level. Any predisposed genetic perturbations in this iron-calcium-Miro axis, which could be due to different rare variants in each person, would further exacerbate its dysfunction. With or without another trigger such as a virus infection or environmental insult, the tipping point for disease onset might be reached. Thus, combining complementary genetic and functional studies may help us better understand the destructive paths leading to the disease and identify network hubs for therapeutic targeting.

Screening people for genetic variants in this iron-calcium-Miro axis and detecting Miro in blood cells may help stratify a unique population of patients and at-risk individuals, who will particularly benefit from therapeutic interventions targeting this axis. For example, treating people bearing genetic variants in Ca^{2+}-channels with Ca^{2+}-channel blockers, iron-chelators, or both, may yield the best efficacy. Similarly, people who test positive for the Miro1 phenotype in PBMCs may respond best to drugs reducing Miro1. Integrating genetic screening of this axis with Miro1 detection in peripheral tissues may enhance the accuracy of risk evaluation and help design personalized treatment, such as a cocktail of different Ca^{2+}-channel blockers, iron chelators, and Miro reducers, to improve prevention and treatment efficacy.

Calcium mishandling and iron accumulation have been widely observed in PD neurons (Angelova et al., 2020; Apicco et al., 2021; Belaidi and Bush, 2016; Buttner et al., 2013; Kim et al., 2020; Lee et al., 2018; Surmeier et al., 2017; Tabata et al., 2018; Verma et al., 2017; Vuuren et al., 2020). Now we have provided a mechanistic link. Fe^{2+} elicits mitochondrial Ca^{2+}-overload through acting on IMM Ca^{2+}-channels and transporters. Further investigations are needed to dissect how Fe^{2+} regulates MCUb and NCLX levels. One hypothesis is that these proteins are targeted by Ca^{2+}-activated mitochondrial proteases. Our results (Figure 6J) have suggested that Fe^{2+}-triggered Ca^{2+}-efflux delay depends on mitochondrial Ca^{2+}-overload. A recent study has shown that NCLX protein levels are lowered in another mitochondrial iron-dependent

disease, Friedreich's Ataxia (FA), through a possible mechanism dependent on calpain cleavage (Britti et al., 2021). Intriguingly, iron chelators have displayed promising therapeutic benefits in preclinical models of both PD (Clark et al., 2020) and FA (Llorens et al., 2019), and is currently in multiple clinical trials for treating symptoms of PD patients (Clark et al., 2020). Thus, the underlying molecular mechanisms may be shared by multiple diseases with mitochondrial iron accumulation.

The consequences to intracellular Ca^{2+}-dysfunction could be profound and detrimental. Dissecting these downstream details in PD will help us find more powerful targets and biomarkers. Mitochondrial Ca^{2+}-overload could overwhelm the oxidative phosphorylation system (Ashrafi et al., 2020), damaging the electron transport chain. Malfunctions of MCU and NCLX may disrupt spatially discrete Ca^{2+} transients and oscillations adjacent to ER membranes, leading to defects in autophagy (Zheng et al., 2022), which may consequently cause protein aggregation and lysosomal dysfunction. Intriguingly, chelating iron can induce selective autophagy pathways (Wilhelm et al., 2022), raising the question whether MCU and local Ca^{2+} dynamics are involved in iron-mediated autophagy. Ca^{2+} may be also important for safeguarding mitochondrial quality. Miro appears to be a molecular switch between distinct routes of mitochondrial quality control. Proteasomal degradation of Miro dissociates mitochondria from microtubules and allows the entire damaged mitochondria to enter the mitophagy pathway (Chan et al., 2011; Hsieh et al., 2016; Wang et al., 2011), whereas sustaining Miro on the microtubule motors is required for the biogenesis of mitochondrial derived vesicles (MDVs) that deliver a subset of mitochondrial proteins (including Miro) to lysosomes (Konig et al., 2021). Notably, MDVs occur under mild oxidative stress or at steady state, and before mitophagy which is triggered by extended damage (Konig et al., 2021; Lin et al., 2017; McLelland et al., 2014). Miro may also ride with those damaged mitochondria expelled from neurons through nanotunnels and vesicles (Ahmad et al., 2014; Davis et al., 2014; Melentijevic et al., 2017; Rosina

et al., 2022; Saha et al., 2022). Perhaps it starts with only one of these biological processes impaired by Ca^{2+} signals, leading to Miro retention on damaged mitochondria, which further affects more Miro-dependent quality control pathways. More studies are needed to unravel the precise roles of Miro and other Ca^{2+}-binding proteins in PD pathogenesis and how Ca^{2+} regulates these roles. The physical and functional interactions of these Ca^{2+}-binding proteins with specific Ca^{2+}-channels in plasma, mitochondrial, or additional organellar membranes, may constitute the core underlying mechanisms.

REFERENCES

Ahmad, T., Mukherjee, S., Pattnaik, B., Kumar, M., Singh, S., Kumar, M., Rehman, R., Tiwari, B.K., Jha, K.A., Barhanpurkar, A.P., *et al.* (2014). Miro1 regulates intercellular mitochondrial transport & enhances mesenchymal stem cell rescue efficacy. The EMBO journal *33*, 994-1010.

Angelova, P.R., Choi, M.L., Berezhnov, A.V., Horrocks, M.H., Hughes, C.D., De, S., Rodrigues, M., Yapom, R., Little, D., Dolt, K.S., *et al.* (2020). Alpha synuclein aggregation drives ferroptosis: an interplay of iron, calcium and lipid peroxidation. Cell death and differentiation *27*, 2781-2796.

Apicco, D.J., Shlevkov, E., Nezich, C.L., Tran, D.T., Guilmette, E., Nicholatos, J.W., Bantle, C.M., Chen, Y., Glajch, K.E., Abraham, N.A., *et al.* (2021). The Parkinson's disease-associated gene ITPKB protects against alpha-synuclein aggregation by regulating ER-to-mitochondria calcium release. Proceedings of the National Academy of Sciences of the United States of America *118*.

Ashrafi, G., de Juan-Sanz, J., Farrell, R.J., and Ryan, T.A. (2020). Molecular Tuning of the Axonal Mitochondrial Ca(2+) Uniporter Ensures Metabolic Flexibility of Neurotransmission. Neuron *105*, 678-687 e675.

Baughman, J.M., Perocchi, F., Girgis, H.S., Plovanich, M., Belcher-Timme, C.A., Sancak, Y., Bao, X.R., Strittmatter, L., Goldberger, O., Bogorad, R.L., *et al.* (2011). Integrative genomics identifies MCU as an essential component of the mitochondrial calcium uniporter. Nature *476*, 341-345.

Belaidi, A.A., and Bush, A.I. (2016). Iron neurochemistry in Alzheimer's disease and Parkinson's disease: targets for therapeutics. Journal of neurochemistry *139 Suppl 1*, 179-197.

Billesbolle, C.B., Azumaya, C.M., Kretsch, R.C., Powers, A.S., Gonen, S., Schneider, S., Arvedson, T., Dror, R.O., Cheng, Y., and Manglik, A. (2020). Structure of hepcidin-bound ferroportin reveals iron homeostatic mechanisms. Nature *586*, 807-811.

Britti, E., Delaspre, F., Tamarit, J., and Ros, J. (2021). Calpain-Inhibitors Protect Frataxin-Deficient Dorsal Root Ganglia Neurons from Loss of Mitochondrial Na(+)/Ca(2+) Exchanger, NCLX, and Apoptosis. Neurochem Res *46*, 108-119.

Buttner, S., Faes, L., Reichelt, W.N., Broeskamp, F., Habernig, L., Benke, S., Kourtis, N., Ruli, D., Carmona-Gutierrez, D., Eisenberg, T., *et al.* (2013). The Ca2+/Mn2+ ion-pump PMR1 links elevation of cytosolic Ca(2+) levels to alpha-synuclein toxicity in Parkinson's disease models. Cell death and differentiation *20*, 465-477.

494 Chan, N.C., Salazar, A.M., Pham, A.H., Sweredoski, M.J., Kolawa, N.J., Graham, R.L., Hess, S., and
495 Chan, D.C. (2011). Broad activation of the ubiquitin-proteasome system by Parkin is critical for
496 mitophagy. Human molecular genetics *20*, 1726-1737.
497 Clark, E.H., Vazquez de la Torre, A., Hoshikawa, T., and Briston, T. (2020). Targeting mitophagy in
498 Parkinson's disease. The Journal of biological chemistry.
499 Darakhshan, S., and Pour, A.B. (2015). Tranilast: a review of its therapeutic applications. Pharmacol
500 Res *91*, 15-28.
501 Davis, C.H., Kim, K.Y., Bushong, E.A., Mills, E.A., Boassa, D., Shih, T., Kinebuchi, M., Phan, S.,
502 Zhou, Y., Bihlmeyer, N.A.*, et al.* (2014). Transcellular degradation of axonal mitochondria. Proceedings
503 of the National Academy of Sciences of the United States of America *111*, 9633-9638.
504 Diaz-Ortiz, M.E., Seo, Y., Posavi, M., Carceles Cordon, M., Clark, E., Jain, N., Charan, R., Gallagher,
505 M.D., Unger, T.L., Amari, N.*, et al.* (2022). GPNMB confers risk for Parkinson's disease through
506 interaction with alpha-synuclein. Science *377*, eabk0637.
507 Dong, Z., Shanmughapriya, S., Tomar, D., Siddiqui, N., Lynch, S., Nemani, N., Breves, S.L., Zhang, X.,
508 Tripathi, A., Palaniappan, P.*, et al.* (2017). Mitochondrial Ca(2+) Uniporter Is a Mitochondrial Luminal
509 Redox Sensor that Augments MCU Channel Activity. Molecular cell *65*, 1014-1028 e1017.
510 Fan, C., Fan, M., Orlando, B.J., Fastman, N.M., Zhang, J., Xu, Y., Chambers, M.G., Xu, X., Perry, K.,
511 Liao, M.*, et al.* (2018). X-ray and cryo-EM structures of the mitochondrial calcium uniporter. Nature
512 *559*, 575-579.
513 Fan, M., Zhang, J., Tsai, C.W., Orlando, B.J., Rodriguez, M., Xu, Y., Liao, M., Tsai, M.F., and Feng, L.
514 (2020). Structure and mechanism of the mitochondrial Ca(2+) uniporter holocomplex. Nature *582*, 129-
515 133.
516 Ghosh, S., Basu Ball, W., Madaris, T.R., Srikantan, S., Madesh, M., Mootha, V.K., and Gohil, V.M.
517 (2020). An essential role for cardiolipin in the stability and function of the mitochondrial calcium
518 uniporter. Proceedings of the National Academy of Sciences of the United States of America *117*,
519 16383-16390.
520 Hsieh, C.H., Li, L., Vanhauwaert, R., Nguyen, K.T., Davis, M.D., Bu, G., Wszolek, Z.K., and Wang, X.
521 (2019). Miro1 Marks Parkinson's Disease Subset and Miro1 Reducer Rescues Neuron Loss in
522 Parkinson's Models. Cell metabolism *30*, 1131-1140 e1137.
523 Hsieh, C.H., Shaltouki, A., Gonzalez, A.E., Bettencourt da Cruz, A., Burbulla, L.F., St Lawrence, E.,
524 Schule, B., Krainc, D., Palmer, T.D., and Wang, X. (2016). Functional Impairment in Miro Degradation
525 and Mitophagy Is a Shared Feature in Familial and Sporadic Parkinson's Disease. Cell stem cell *19*, 709-
526 724.
527 Katona, M., Bartok, A., Nichtova, Z., Csordas, G., Berezhnaya, E., Weaver, D., Ghosh, A., Varnai, P.,
528 Yule, D.I., and Hajnoczky, G. (2022). Capture at the ER-mitochondrial contacts licenses IP(3) receptors
529 to stimulate local Ca(2+) transfer and oxidative metabolism. Nature communications *13*, 6779.
530 Kim, J.W., Yin, X., Jhaldiyal, A., Khan, M.R., Martin, I., Xie, Z., Perez-Rosello, T., Kumar, M.,
531 Abalde-Atristain, L., Xu, J.*, et al.* (2020). Defects in mRNA Translation in LRRK2-Mutant hiPSC-
532 Derived Dopaminergic Neurons Lead to Dysregulated Calcium Homeostasis. Cell stem cell *27*, 633-645
533 e637.
534 Konig, T., Nolte, H., Aaltonen, M.J., Tatsuta, T., Krols, M., Stroh, T., Langer, T., and McBride, H.M.
535 (2021). MIROs and DRP1 drive mitochondrial-derived vesicle biogenesis and promote quality control.
536 Nature cell biology.
537 Lambert, J.P., Luongo, T.S., Tomar, D., Jadiya, P., Gao, E., Zhang, X., Lucchese, A.M., Kolmetzky,
538 D.W., Shah, N.S., and Elrod, J.W. (2019). MCUB Regulates the Molecular Composition of the

539 Mitochondrial Calcium Uniporter Channel to Limit Mitochondrial Calcium Overload During Stress.
540 Circulation *140*, 1720-1733.
541 Lee, K.S., Huh, S., Lee, S., Wu, Z., Kim, A.K., Kang, H.Y., and Lu, B. (2018). Altered ER-
542 mitochondria contact impacts mitochondria calcium homeostasis and contributes to neurodegeneration
543 in vivo in disease models. Proceedings of the National Academy of Sciences of the United States of
544 America *115*, E8844-E8853.
545 Lee, S.K., Shanmughapriya, S., Mok, M.C.Y., Dong, Z., Tomar, D., Carvalho, E., Rajan, S., Junop,
546 M.S., Madesh, M., and Stathopulos, P.B. (2016). Structural Insights into Mitochondrial Calcium
547 Uniporter Regulation by Divalent Cations. Cell Chem Biol *23*, 1157-1169.
548 Li, L., Conradson, D.M., Bharat, V., Kim, M.J., Hsieh, C.H., Minhas, P.S., Papakyrikos, A.M., Durairaj,
549 A.S., Ludlam, A., Andreasson, K.I.*, et al.* (2021). A mitochondrial membrane-bridging machinery
550 mediates signal transduction of intramitochondrial oxidation. Nat Metab.
551 Lin, M.Y., Cheng, X.T., Tammineni, P., Xie, Y., Zhou, B., Cai, Q., and Sheng, Z.H. (2017). Releasing
552 Syntaphilin Removes Stressed Mitochondria from Axons Independent of Mitophagy under
553 Pathophysiological Conditions. Neuron *94*, 595-610 e596.
554 Lin, Y.F., Cheng, C.W., Shih, C.S., Hwang, J.K., Yu, C.S., and Lu, C.H. (2016). MIB: Metal Ion-
555 Binding Site Prediction and Docking Server. J Chem Inf Model *56*, 2287-2291.
556 Llorens, J.V., Soriano, S., Calap-Quintana, P., Gonzalez-Cabo, P., and Molto, M.D. (2019). The Role of
557 Iron in Friedreich's Ataxia: Insights From Studies in Human Tissues and Cellular and Animal Models.
558 Front Neurosci *13*, 75.
559 Lu, C.H., Lin, Y.F., Lin, J.J., and Yu, C.S. (2012). Prediction of metal ion-binding sites in proteins using
560 the fragment transformation method. PloS one *7*, e39252.
561 McLelland, G.L., Soubannier, V., Chen, C.X., McBride, H.M., and Fon, E.A. (2014). Parkin and PINK1
562 function in a vesicular trafficking pathway regulating mitochondrial quality control. The EMBO journal
563 *33*, 282-295.
564 Melentijevic, I., Toth, M.L., Arnold, M.L., Guasp, R.J., Harinath, G., Nguyen, K.C., Taub, D., Parker,
565 J.A., Neri, C., Gabel, C.V.*, et al.* (2017). C. elegans neurons jettison protein aggregates and
566 mitochondria under neurotoxic stress. Nature *542*, 367-371.
567 Munson, M.J., Mathai, B.J., Ng, M.Y.W., Trachsel-Moncho, L., de la Ballina, L.R., Schultz, S.W.,
568 Aman, Y., Lystad, A.H., Singh, S., Singh, S.*, et al.* (2021). GAK and PRKCD are positive regulators of
569 PRKN-independent mitophagy. Nature communications *12*, 6101.
570 Nalls, M.A., Blauwendraat, C., Vallerga, C.L., Heilbron, K., Bandres-Ciga, S., Chang, D., Tan, M., Kia,
571 D.A., Noyce, A.J., Xue, A.*, et al.* (2019). Identification of novel risk loci, causal insights, and heritable
572 risk for Parkinson's disease: a meta-analysis of genome-wide association studies. The Lancet Neurology
573 *18*, 1091-1102.
574 Nguyen, D., Bharat, V., Conradson, D.M., Nandakishore, P., and Wang, X. (2021). Miro1 Impairment in
575 a Parkinson's At-Risk Cohort. Front Mol Neurosci *14*, 734273.
576 Ordureau, A., Paulo, J.A., Zhang, J., An, H., Swatek, K.N., Cannon, J.R., Wan, Q., Komander, D., and
577 Harper, J.W. (2020). Global Landscape and Dynamics of Parkin and USP30-Dependent Ubiquitylomes
578 in iNeurons during Mitophagic Signaling. Molecular cell *77*, 1124-1142 e1110.
579 Palty, R., Silverman, W.F., Hershfinkel, M., Caporale, T., Sensi, S.L., Parnis, J., Nolte, C., Fishman, D.,
580 Shoshan-Barmatz, V., Herrmann, S.*, et al.* (2010). NCLX is an essential component of mitochondrial
581 Na+/Ca2+ exchange. Proceedings of the National Academy of Sciences of the United States of America
582 *107*, 436-441.

583 Patron, M., Tarasenko, D., Nolte, H., Kroczek, L., Ghosh, M., Ohba, Y., Lasarzewski, Y., Ahmadi, Z.A.,
584 Cabrera-Orefice, A., Eyiama, A.*, et al.* (2022). Regulation of mitochondrial proteostasis by the proton
585 gradient. The EMBO journal *41*, e110476.
586 Rosina, M., Ceci, V., Turchi, R., Chuan, L., Borcherding, N., Sciarretta, F., Sanchez-Diaz, M., Tortolici,
587 F., Karlinsey, K., Chiurchiu, V.*, et al.* (2022). Ejection of damaged mitochondria and their removal by
588 macrophages ensure efficient thermogenesis in brown adipose tissue. Cell Metab.
589 Saha, T., Dash, C., Jayabalan, R., Khiste, S., Kulkarni, A., Kurmi, K., Mondal, J., Majumder, P.K.,
590 Bardia, A., Jang, H.L.*, et al.* (2022). Intercellular nanotubes mediate mitochondrial trafficking between
591 cancer and immune cells. Nat Nanotechnol *17*, 98-106.
592 Shaltouki, A., Hsieh, C.H., Kim, M.J., and Wang, X. (2018). Alpha-synuclein delays mitophagy and
593 targeting Miro rescues neuron loss in Parkinson's models. Acta Neuropathol *136*, 607-620.
594 Surmeier, D.J., Obeso, J.A., and Halliday, G.M. (2017). Selective neuronal vulnerability in Parkinson
595 disease. Nature reviews Neuroscience *18*, 101-113.
596 Tabata, Y., Imaizumi, Y., Sugawara, M., Andoh-Noda, T., Banno, S., Chai, M., Sone, T., Yamazaki, K.,
597 Ito, M., Tsukahara, K.*, et al.* (2018). T-type Calcium Channels Determine the Vulnerability of
598 Dopaminergic Neurons to Mitochondrial Stress in Familial Parkinson Disease. Stem cell reports *11*,
599 1171-1184.
600 Tomar, D., Dong, Z., Shanmughapriya, S., Koch, D.A., Thomas, T., Hoffman, N.E., Timbalia, S.A.,
601 Goldman, S.J., Breves, S.L., Corbally, D.P.*, et al.* (2016). MCUR1 Is a Scaffold Factor for the MCU
602 Complex Function and Promotes Mitochondrial Bioenergetics. Cell Rep *15*, 1673-1685.
603 Verma, M., Callio, J., Otero, P.A., Sekler, I., Wills, Z.P., and Chu, C.T. (2017). Mitochondrial Calcium
604 Dysregulation Contributes to Dendrite Degeneration Mediated by PD/LBD-Associated LRRK2 Mutants.
605 The Journal of neuroscience : the official journal of the Society for Neuroscience *37*, 11151-11165.
606 Vuuren, M.J.V., Nell, T.A., Carr, J.A., Kell, D.B., and Pretorius, E. (2020). Iron Dysregulation and
607 Inflammagens Related to Oral and Gut Health Are Central to the Development of Parkinson's Disease.
608 Biomolecules *11*.
609 Wang, X., and Schwarz, T.L. (2009). The mechanism of Ca2+ -dependent regulation of kinesin-
610 mediated mitochondrial motility. Cell *136*, 163-174.
611 Wang, X., Winter, D., Ashrafi, G., Schlehe, J., Wong, Y.L., Selkoe, D., Rice, S., Steen, J., LaVoie, M.J.,
612 and Schwarz, T.L. (2011). PINK1 and Parkin target Miro for phosphorylation and degradation to arrest
613 mitochondrial motility. Cell *147*, 893-906.
614 Wilhelm, L.P., Zapata-Munoz, J., Villarejo-Zori, B., Pellegrin, S., Freire, C.M., Toye, A.M., Boya, P.,
615 and Ganley, I.G. (2022). BNIP3L/NIX regulates both mitophagy and pexophagy. The EMBO journal,
616 e111115.
617 Zerbes, R.M., van der Klei, I.J., Veenhuis, M., Pfanner, N., van der Laan, M., and Bohnert, M. (2012).
618 Mitofilin complexes: conserved organizers of mitochondrial membrane architecture. Biological
619 chemistry *393*, 1247-1261.
620 Zheng, Q., Chen, Y., Chen, D., Zhao, H., Feng, Y., Meng, Q., Zhao, Y., and Zhang, H. (2022). Calcium
621 transients on the ER surface trigger liquid-liquid phase separation of FIP200 to specify autophagosome
622 initiation sites. Cell.
623

624

625 **Acknowledgements**

We thank M.F. Tsai for *MCU* KO cells, L. Pallanck for flies, A. E. Medlock, O. Ross, and S. Han for discussion, C. Kwak, Z. T. Cook, D. M. Conradson and J. Panji for technical support, the Steinberg lab for assistance, the Wang lab members for discussion, the Stanford HTBC (RRID: SCR_017794) and D. E. Solow-Cordero for assistance with drug screens, and the SBC, the Stanford Alzheimer's Disease Research Center (ADRC), the Department of Pathology at University of California Los Angeles (UCLA), R. N. Alcalay, Columbia University, and the Michael J. Fox Foundation (MJFF) for providing human tissues and cells. This work was supported by NINDS (RO1NS089583, RO1NS128040-01; X.W.), NIGMS (RO1GM143258; X.W.), NIA (RO1AG060747; M.D.G.), Stanford SPARK and Spectrum SPADA (X.W.), Sanofi iAward (X.W.), the Warren Alpert Foundation (X.W.), the MJFF (021146; X.W.), the Harrington Discovery Institute (X.W.), the Belgian American Education Foundation (R.V.), the Glenn Foundation Postdoctoral Fellowship (L.L.), and the European Union's Horizon 2020 research and innovation program under the Marie Skłodowska-Curie (890650; Y.LG.).

Author contributions

R.V. did drug screens. S.E.R. and R.B.A. performed pathway analysis. V.B., A.S.D., C.-H.H., L.L., and S.C. performed human cell experiments. L.L. conducted fly work. C.M.M. and L.F. did in vitro work. Y.LG. and M.D.G. analyzed human genetic data. P.N. analyzed PBMC data. X.W. conceived and supervised the project. All authors designed the experiments and wrote the paper.

Competing interests

The authors declare the following competing interests: X.W. is a co-founder, adviser, and shareholder of AcureX Therapeutics, and a shareholder of Mitokinin Inc. V.B., L.L., C.-H.H., and R.V. are shareholders of AcureX Therapeutics. P.N. is employed by Vroom Inc. Patents based on this study were filed by

649 Stanford University with X.W., R.V., V.B., L.L., C.-H.H. as inventors. The remaining authors declare no
650 competing interests.
651

652 ## Data availability

653 Further information and reagents are available from the corresponding author.
654

655 **FIGURE LEGENDS**

656 **Figure 1. HTP Screens Identify Ca^{2+}-Related Drug Hits for PD.** (A) Schematic representation of a
657 custom-designed drug screen for Miro1 in PD fibroblasts. (B) Pathway analysis identified calcium as a
658 shared factor in the primary hit-Miro1 network. Each individual pathway is generated using a primary hit
659 and Miro1 as search query and the resulting subnetwork is visualized and curated using docs2graph–a
660 knowledge-graph browser. The visualization shows a subgraph generated by docs2graph from the
661 collection of curated supporting documents for each pathway.
662

663 **Figure 2. Benidipine Rescues PD Relevant Phenotypes.** (A-B) iPSC-derived neurons from a PD patient
664 with *SNCA-A53T* and the isogenic control, treated as indicated, were immunostained with anti-TH (A) or
665 TUNEL and Dapi (B), and imaged under a confocal microscope. Scale bars: 100 μm. Below:
666 Quantifications of the density of TH-positive neurons (A) or the percentage of TUNEL-positive neurons
667 (B). n=20 images from 3 independent coverslips. P values are compared with the far-left bar, except
668 indicated otherwise. (C) 40-day-old fly brains were immunostained with anti-TH and the DA neuron
669 number was counted in the PPL1 cluster. Scale bar: 20 μm. n=4, 7, 7, 4 (from left to right). (D) The
670 Performance Index was measured in 30-day-old flies, fed as indicated. n=59, 57, 54, 57 flies (from left to

671 right), 3 independent experiments. (C-D) Drug treatment was started from adulthood (day 1). One-Way
672 Anova Post Hoc Tukey Test for all panels.
673
674 **Figure 3. The EF-hands of Miro Play a Role in Causing PD Relevant Phenotypes.** (A) Representative
675 still images from live Mito-dsRed and GFP-Miro1 imaging movies of axons of indicated genotypes,
676 following 100 μM Antimycin A treatment. Scale bar: 10 μm. (B) Left: Quantification of the GFP-Miro1
677 intensity at 25 minutes divided by that at 0 minute following 100 μM Antimycin A treatment from the
678 same axonal region. Right: Quantification of the reduction speed of the GFP-Miro1 intensity within 25
679 minutes following 100 μM Antimycin A treatment. (C) Left: Quantification of the Mito-dsRed intensity
680 at 58 minutes divided by that at 0 minute following 100 μM Antimycin A treatment from the same axonal
681 region. Right: Quantification of the Mito-dsRed intensity reduction speed within 58 minutes following
682 100 μM Antimycin A treatment. (B-C) n=5, 4, 5 (from left to right) axons (one axon per coverslip). (D)
683 The DA neuron number was counted in the PPL1 cluster of flies with indicated genotypes. Scale bar: 20
684 μm. n=7, 4, 6, 5 (from left to right). (E) The Performance Index was measured in flies with indicated
685 genotypes and age. n (from left to right)=49, 47, 40, 47 flies (day 12); 49, 47, 39, 47 (day 14); 48, 45, 37,
686 44 (day 20); 3 independent experiments. One-Way Anova Post Hoc Tukey Test for all panels.
687
688 **Figure 4. PD Mitochondria Import More Ca^{2+}.** iPSC-derived neurons from a PD patient with *SNCA-*
689 *A53T* and the isogenic control were stimulated with thrombin and mitochondrial (Rhod-2) and cytosolic
690 Ca^{2+} levels (Calcium Green) were measured. Left: Representative traces of Ca^{2+} ions in neurons. Right:
691 Quantifications of the peak fluorescent intensity normalized to baseline. n=15 cell bodies from 3
692 independent coverslips. Two-tailed Welch's T Test.
693

694 **Figure 5. Iron Promotes MCU Oligomerization.** (A) Elution profiles of MCU from SEC samples. (B)
695 HEK cells were treated similarly as above, run in Native-PAGE, and blotted. Right: Qualifications of the
696 band intensities normalized to the total protein amount measured by BCA. n=5 independent experiments.
697 One-Way Anova Post Hoc Tukey Test. (C) Elution profiles of additional proteins from SEC samples.
698
699 **Figure 6. MCU Binds to Fe^{2+}.** (A) HEK cells were treated with or without 5 mM Fe^{2+} for 21 hours, then
700 IPed with rabbit IgG or anti-MCU, and Fe^{2+} concentrations in the IP samples were detected. n=4
701 independent experiments. Top western blots demonstrated the success of IP. Anti-MCU was validated
702 using *MCU-/-* HEK cell lysate (bottom panel). Arrow indicates the MCU band. (B) HEK cells were treated
703 with 5 mM Fe^{2+} or Co^{2+} for 22 hours and lysed in buffer containing the same metal. Lysates were run in
704 Native- or SDS-PAGE and blotted with anti-MCU. Similar results were seen for at least 3 times. (C) HEK
705 cells treated with 5 mM Fe^{2+} or 500 μM Co^{2+} for 22 hours were stimulated with thrombin and
706 mitochondrial Ca^{2+} levels (Rhod-2) were measured. The peak fluorescent intensity normalized to baseline
707 is quantified. n=20 cells from 4 independent coverslips. (D-E) Fluorescence-detection SEC profiles of
708 purified human MCU. The annotation of the peaks is based on (Fan et al., 2018; Fan et al., 2020). (F)
709 *MCU-/-* HEK cells transfected as indicated were treated with 5 mM Fe^{2+} for 20 hours, then IPed with anti-
710 Flag, and Fe^{2+} concentrations in the IP samples were detected. Two-tailed paired T Test. (G) Left:
711 Representative blots of IP with anti-Flag using cell lysates as indicated, run in Native- or SDS-PAGE.
712 Right: Quantification of the band intensity of MCU-Flag in Native-PAGE normalized to that in SDS-
713 PAGE from the same experiment. n=4 independent experiments. (H) HEK cells treated as indicated were
714 stimulated with thrombin and mitochondrial Ca^{2+} levels (Rhod-2) were measured. Representative traces
715 of Ca^{2+} ions. (I-J) Based on traces like in (H), the peak fluorescent intensity normalized to baseline (I) or

efflux rate (J) is quantified. n=17 cells from 4 independent coverslips. Two-tailed Welch's T Test for all panels except (F).

Figure 7. Chelating Iron Restores Ca^{2+} and neuronal homeostasis in PD neurons. (A) Similar to Figure 4, iPSC-derived neurons from a PD patient with *SNCA-A53T* and the isogenic control, with or without treatment of 100 μM DFP for 24 hours, were stimulated with thrombin, and mitochondrial Ca^{2+} (Rhod-2) was measured. Quantifications of the peak fluorescent intensity normalized to baseline. n=15 cell bodies from 3 independent coverslips. Control data without DFP treatment are the same as in Figure 4. One-Way Anova Post Hoc Tukey Test. (B) iPSC-derived neurons treated as indicated, were immunostained with TUNEL and Dapi, and imaged under a confocal microscope. Scale bar: 50 μm. Below: Quantification of the percentage of TUNEL-positive neurons. n=20 images from 3 independent coverslips. P values are compared within each genotype (significant compared to every other condition) with One-Way Anova Post Hoc Tukey Test. (C) The DA neuron number was counted in the PPL1 cluster of flies with indicated genotypes and conditions. Drug treatment was started from adulthood (day 1). Scale bar: 20 μm. n=6, 9, 8, 7 (from left to right). (D) The Performance Index was measured in flies. Drug treatment was started from embryogenesis. n=35, 33, 40, 34 flies (from left to right), 3 independent experiments. (C-D) One-Way Anova Post Hoc Tukey Test. (E) Postmortem brains were run in Native- or SDS-PAGE and blotted. The band intensity normalized to the total protein level measured by BCA is divided by that of the universal control on the same blot: CVD (cardiovascular disease), which was included on every blot. The MCU oligomer bands in Native-PAGE and the NCLX and MCUb bands in SDS-PAGE (average of 3 replicates) are used in the plot. HC: healthy control. (F) Miro1 protein levels were measured using ELISA in PBMCs treated with DMSO or 40 μM CCCP for 6 hours. Miro1 Ratio is calculated by dividing the Miro1 value treated with CCCP by that with DMSO from the same subject. Dot

739 plot with Mean±S.E.M. n=80 healthy controls and 107 PD. Two-tailed Welch's T Test. (G) PBMCs from
740 4 PD patients were treated with 40 μM CCCP for 6 hours, or pretreated with 10 μM Benidipine or MR3
741 for 18 hours and then with 40 μM CCCP for another 6 hours, and Miro1 protein was detected using ELISA.
742 Patient IDs are the same as in Table S4. Two-tailed paired T Test. (H) Schematic representation of the
743 iron-calcium-Miro axis discovered in this study. Red texts show genes containing variants associated with
744 PD status.
745
746